



Wear Maps and Statistical Approach of AISI 316L Alloy under Dry Sliding Conditions

R.A. García-León , J. Martínez-Trinidad, A. Guevara-Morales, I. Campos-Silva, and U. Figueroa-López

Submitted: 15 March 2021 / Revised: 12 April 2021 / Accepted: 17 April 2021 / Published online: 11 May 2021

In the present work, 2D wear maps and statistical approaches on commercial samples of AISI 316L stainless steel were obtained to provide a general visualization of response variables and wear regimes under different dry sliding conditions. Dry sliding wear tests on the AISI 316L steel were performed according to the ASTM G133-05 standard procedure guidelines. A linear reciprocating sliding tribometer with a ball-on-flat configuration and a counterpart of Al_2O_3 was used. Wear tests were performed at room temperature with the following conditions: sliding distance of 100 m, a constant applied load of 5, 10, and 20 N, and sliding speeds of 5, 10, 20, and 30 mm/s. The analysis of variance showed that the load influences the depth, volume, and CoF response variables in a positive way with more than 97% of confidence; while the specific wear rate response variable is mainly affected by the sliding speed with more than 42% of confidence. 2D maps of the response variables were obtained using response surface methodology as a function of the load and sliding speed. The maximum specific wear rate was $\sim 450 \times 10^{-6} \text{ mm}^3/\text{Nm}$ for the condition of 5 N and 5 mm/s, influenced by the test conditions. From SEM analysis, wear regimes were classified as mild and severe and thus plowing, and material agglomeration predominate as failure mechanisms during mild wear. For severe wear, differences are more evident, with smearing being predominant on the worn tracks.

Keywords AISI 316L stainless steel, failure mechanisms, wear maps, wear resistance, wear regimes

1. Introduction

AISI 316L is an ultra-low carbon stainless steel with a chemical composition of nickel, chromium, molybdenum, and manganese, which improves its response to pitting in chlorinated environments, and good corrosion resistance at high temperatures. This stainless steel is one of the most used materials in biomedical applications, due to the chemical composition, biocompatibility and low cost (Ref 1). Biomedical components can be subject to different tribological parameters such as loads, speeds, and environments; these parameters are analyzed to improve the tribological behavior (Ref 2, 3).

Wear is defined as the progressive loss of material due to relative motion at the surface under different test parameters (Ref 4). This phenomenon could be improved by applied thermal or thermochemical treatments that reducing the damage generated on the surface of the material. Because there are several wear mechanisms that change in relative importance as the operating conditions are changed, and no single wear mechanism operates over a wide range of conditions, wear maps are a useful tool for explaining the role of the operating environment on wear mechanisms (Ref 5, 6, 7). Several

regimes of wear for a particular test configuration can appear on a single wear regime map plotted on axes of sliding speed, pressure, load, among others (Ref 8, 9). This will allow predicting, evaluate and optimize wear behavior in terms of operating conditions.

Wear maps, and statistical approach of different materials has been reported in different ways. Davanageri et al. (Ref 10) evaluated the effects of the independent parameters such as load, distance, and sliding speed on the wear performance of the heat-treated super duplex AISI 2507 stainless steel under pin-on-disk configuration. The statistical analysis showed that the specific wear rate is affected by the wear parameters; in this way, the applied load was found to have a major significance, followed by the speed and sliding distance. Basavarajappa and Chandramohan (Ref 11) evaluated the influence of independent parameters on the wear volume removal of metal matrix composites through the pin-on-disk wear test under dry sliding conditions. In the same way, Baskaran and Anandkrishnan (Ref 12) performed the statistical analysis and mathematical modeling of the coefficient of friction under dry sliding conditions using a pin-on-disk test for the reinforced aluminum metal matrix composites. Bassiouny Saleh et al. (Ref 13) developed a statistical analysis of dry sliding wear parameters of the AZ91 alloy; the response surface methodology was used to compare and optimize the weight loss response variable on the wear failure mechanisms (Ref 14).

For the case of the AISI 316L stainless Steel, Montes-Seguedo et al. (Ref 15) reported the wear maps on the coefficient of friction under lubricated conditions on commercial samples of AISI 316L using a pin-on-disk wear test. Peruzzo et al. (Ref 16) studied the tribological behavior of the AISI 316L stainless steels with boron additions. O'Donnell et al. (Ref 17) plotted wear maps as a function of load and sliding speed on hardened 316L austenitic stainless steel carburized at low temperatures using pin-on-disk under dry sliding wear tests. Farias et al. (Ref 18) evaluated the sliding

R.A. García-León, J. Martínez-Trinidad, and I. Campos-Silva, Instituto Politécnico Nacional, Grupo Ingeniería de Superficies, SEPI-ESIME Zacatenco, 07738 Mexico City, Mexico; and A. Guevara-Morales and U. Figueroa-López, Tecnológico de Monterrey, Escuela de Ingeniería y Ciencias, 52926 Atizapán de Zaragoza, Estado de Mexico, Mexico. Contact e-mails: ragarcial@ufps.edu.co and jomartinez@ipn.mx.

wear behavior of two stainless steel (AISI 304 and AISI 316) under different loads and speeds using commercial pin-on-disk equipment. The experimental values obtained were plotted with response surface methodology. The results showed that plasticity dominated wear, and that failure mechanisms such as metallic particle oxidation, adhesive wear, and mixed wear appear. Also, the specific wear rate was dependent on the interaction between the applied load and sliding speed, and thus, a change in the wear mechanism was associated with the test parameters. García-León et al. (Ref 19, 20) reported wear maps for the borided AISI 316L stainless steel under dry sliding conditions using a ball-on-flat configuration to provide a general visualization of the wear performance; also, and statistical study was developed to provide information about the significance of the response variable taking into account the factors and levels applied during sliding wear. The results showed that the load had the major statistical significance with the 63.7% of importance on the specific wear rate.

In the literature, 2D wear maps for AISI 316L stainless steel and the statistical approach of the variable response under dry sliding conditions during ball-on-flat test configuration have not been reported. In this study, 2D wear maps are developed on AISI 316L steel with the aim of providing a general visualization of the behavior of the specific wear rate and wear regimes as a function of dry sliding conditions (i.e., load and sliding speed of the test) in a ball-on-flat configuration test for biomedical applications.

2. Experimental Procedures

2.1 Preparation of the AISI 316L Samples

20 mm diameter and 2 mm thick cylindrical samples of austenitic AISI 316L stainless steel were cut, such as shown in

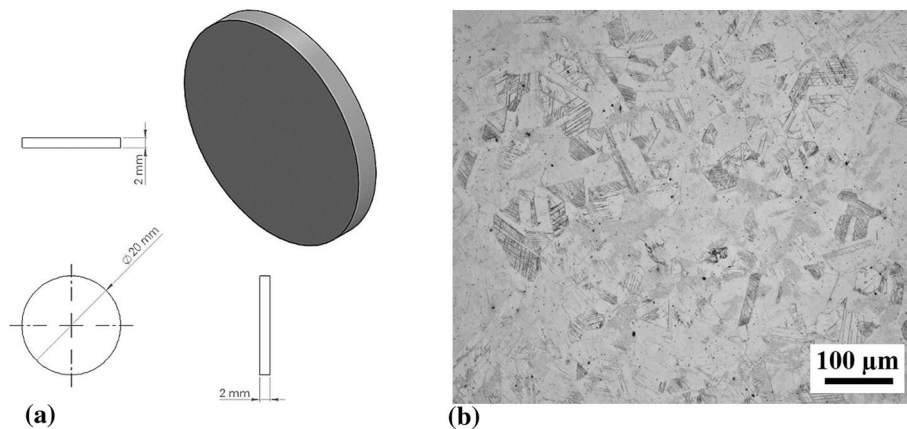


Fig. 1 (a) Sample geometry, and (b) Microstructure of the AISI 316L stainless steel

Table 1 Nominal chemical composition (wt. %) of AISI 316L stainless steel (Ref 22)

Element								
Cr	Ni	Mo	Mn	Si	P	C	S	Fe
16-18	10-15	2-3	2 max.	1 max.	0.04 max.	0.03 max.	0.03 max.	Balanced

Fig. 1(a). The microstructure of the AISI 316L steel was revealed using Nital 2%, note that the presence of macles and chromium precipitates was evident due to the alloy's austenitic structure, as shown in Fig. 1(b) obtained via optical microscopy. The chemical composition for the stainless steel used is shown in Table 1. Further, samples presented a surface hardness of ~ 2.1 GPa measured by Vickers microindentation, with Young's modulus of ~ 210 GPa (Ref 21)).

2.2 Dry Wear Test

Wear tests on the AISI 316L stainless steel were performed at room temperature (25 °C) and 50% relative humidity using a Bruker/UMT-2 universal tester under ball-on-flat dry sliding conditions (Fig. 2) in a stroke length of 10 mm. Prior to wear tests, all the samples were metallographically prepared (abrasive paper and polished) until obtaining a surface roughness less than $R_a \leq 0.05 \mu\text{m}$ according to ASTM G133-05 standard procedure. Al_2O_3 balls ($\phi=6$ mm, $H = 22$ GPa, $E = 350$ GPa, and $\nu = 0.30$) were selected as counterpart as it is the most widely used ceramic material in bio-tribological applications (implants for biomedical applications). Also, Al_2O_3 balls present an ultra-low specific wear rate under sliding (Ref 23).

During the wear tests, the coefficient of friction (CoF) was continually recorded with the aid of the Bruker/CETR software. The experimental conditions and contact mechanic parameters of the wear tests are shown in Table 2; note that, at least three replicate tests were performed for each experimental condition to guaranty the statistical quality of the results.

After the wear tests, the volume of material removed (V) was obtained across the wear tracks by non-contact profilometry with the aid of the Bruker/Contour GT-K 3D instrument, and the specific wear rate (k) was estimated with Eq 1, where P is the applied normal load and S is the total sliding distance (Ref 24).

$$k = \frac{V}{P \times S}, \left(\frac{\text{mm}^3}{\text{N} \times \text{m}} \right) \quad (\text{Eq 1})$$

Finally, the failure mechanisms and the chemical composition over the surface of the worn tracks, developed for the overall experimental conditions were analyzed via SEM/EDS using a JEOL/JSM-7800F instrument at 5 kV.

2.3 Statistical Experimental Design

The statistical approximation of the wear test parameters such as load (L) and speed (S) on the response variables which are the depth (D), volume (V), specific wear rate (k), and CoF, were estimated (Ref 12, 25). As a product of the combination of factors L, and S with three levels each one, 9 tests were developed through a factorial 3² in a completely randomized design (CRD) with three replicate tests (Table 2).

The AV or ANOVA analysis of variance was applied to the experimental factors and response variables on the wear test

with the aid of the Stargraphics Centurion software (Ref 26). ANOVA is a statistical technique that is useful to analyze the total variation of the experimental results of a particular design, decomposing it into independent sources of variation attributable to each of the effects that conform to the experimental design (Ref 27). The significance of the model terms were identified through the p values ($p \leq 0.05$). In this way, was applied the methodology or steps showed in Fig. 3.

A recommendation for experimenters is to always analyze experimental goals and define clear related and measurable response variables. In the same direction, potential design and problem factors must be analyzed and adequately treated. Experimenters can consider sequential experiments in more than the 2 proposed steps, starting with the mixed design and then analyzing other design factors with a 3^K family experiments prior to characterizations experiments. This approximation is more straightforward but cannot explore other regions with different compositions. Trade-off differs per context and researcher.

2.4 Construction of Wear Maps

The Response Surface Methodology (RSM) modulus and DWSL fitting on Statistica software was used to obtain 2D wear maps of the response variables. These response surfaces, or maps, are a geometric representation obtained by plotting response variables (e.g., CoF, depth, specific wear rate) as a function of one or more quantitative independent factors (e.g., load, sliding speed, total sliding distance). Maps were obtained with the aim of providing a global visualization of the material wear performance under different dry sliding conditions (Ref 28). This is a useful tool that allows evaluating the effect of multiple factors and interactions on the response variable, and thus, determine design factor settings to improve or optimize the response. Basically, Statistica software performs a quadratic regression analysis based on experimental values to obtain the response surface.

3. Results

The experimental values were collected according to the 3^K statistical design to investigate the statistical assumptions and correlations using RSM. The response variables predictions were estimated using ANOVA analysis of variance using the response equation that governs the RSM plots through validating the percentage of correlation, taking into account the experimental values obtained.

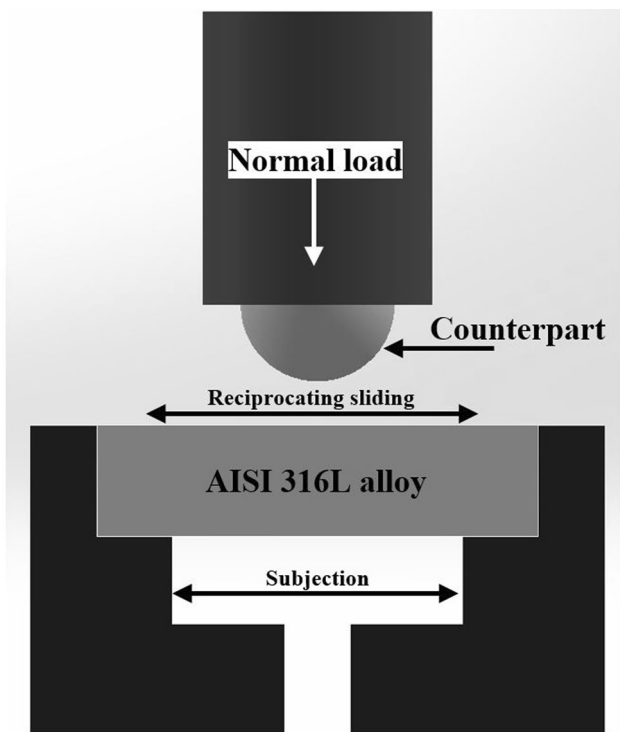


Fig. 2 Schematic diagram of the linear reciprocating wear test using the UMT-2 tribometer

Table 2 Contact mechanics parameters obtained for the experimental conditions on the AISI 316L stainless steel

Sample	Factor levels	Factors			Contact mechanic parameters			
		Sliding speed, mm/s	Applied load, N	Total sliding distance, m	Max. contact pressure, GPa	Max. shear stress, MPa	Depth of max. shear stress, μm	Contact radius, mm
AISI 316L	1	10	5	100	1.37	425.1	20.02	0.041
	2	20	10		1.72	535.6	25.23	0.052
	3	30	20		2.17	674.8	31.79	0.066

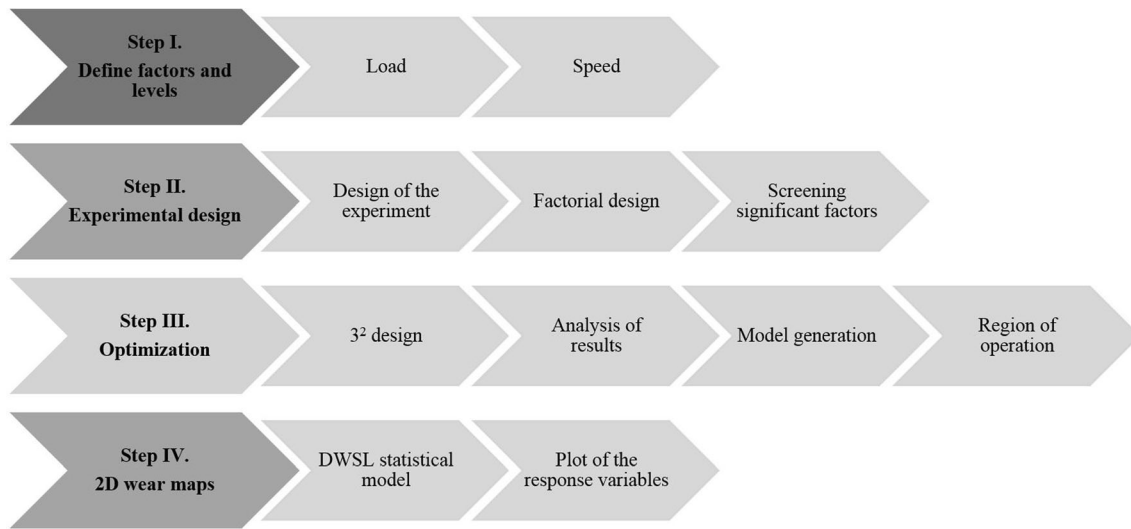


Fig. 3 Methodology and statistical steps used

Table 3 Experimental factors and response variables on wear test

Factors			Experimental values/Response variables			
S	D	L	Depth, D	Volume, V	Specific wear rate (<i>k</i>)	CoF
mm/s	m	N	μm	(mm ³)×10 ⁻³	(mm ³ /Nm)×10 ⁻⁶	
10 [-1]	100	5 [-1]	27.67 ± 1.30	192.6 ± 11.9	385.0 ± 19.40	0.73 ± 0.005
		10 [0]	39.67 ± 0.72	318.0 ± 8.11	318.1 ± 13.21	0.66 ± 0.030
		20 [1]	60.89 ± 1.36	583.4 ± 27.5	291.7 ± 4.49	0.59 ± 0.017
20 [0]	100	5 [-1]	29.00 ± 1.03	149.5 ± 3.84	299.1 ± 6.27	0.65 ± 0.047
		10 [0]	39.00 ± 1.23	275.4 ± 15.5	275.4 ± 2.52	0.56 ± 0.042
		20 [1]	58.78 ± 0.86	502.6 ± 19.5	251.3 ± 3.18	0.51 ± 0.034
30 [1]	100	5 [-1]	27.00 ± 1.10	112.0 ± 9.11	224.0 ± 14.9	0.63 ± 0.062
		10 [0]	38.78 ± 0.86	233.9 ± 11.3	233.9 ± 18.5	0.54 ± 0.047
		20 [1]	58.33 ± 1.54	511.9 ± 22.3	256.0 ± 16.4	0.52 ± 0.036

S is the sliding speed, D is the total distance of sliding, and L is the applied load

3.1 Statistical Results

The levels of the factors were marked as low [-1], medium [0], and high [1] to develop the statistical assumptions, such as shown in Table 3. Note that the sliding distance is constant with a value of 100 m for the overall experimental set of tests.

3.1.1 Screening Analysis. Initially, two levels of each experimental factor were taken for the analysis of variance for the screening design; Table 4 shows that all the factors were significant in the wear test with a $p \leq 0.05$ except with a confidence level of 95%; notice that, for the response variable CoF the interaction between the load and speed has negative variable significance. The response variables studied present a correlation coefficient greater than 99% except for the CoF variables, being highly significant; likewise, the values of the standard error and absolute mean error are observed.

The Durbin-Watson (DW) statistic tests the residuals to determine if there is any significant correlation based on the order in which the experimental values are presented. Since the

$p \geq 5.0\%$, there is no indication of serial autocorrelation in the residuals with a significance level of 5.0%.

Figure 4 shows the screening analysis for the design factors where the statistical significance of the factors in the test was determined. Figure 4(a) and (b) shows that the applied load (B:L) is the factor that most influences the depth of wear in a positive way, that is, the higher the load, the greater the depth; while the speed (A:S) and the second-order interaction of the factors (AB) negatively influence the depth, that is, the higher the speed and the higher load, the lower the depth of wear, the volume of material removal, and therefore the specific wear rate, as has been reported by (Ref 10, 20). Material removal is directly influenced by the load, and thus the volume increase linearly with the load, with adhesive wear mode (Ref 29).

The specific wear rate is not significantly affected by the load, notice that in the case of speed (A:S), it has a negative influence, but the interaction between both factors does have a significant effect on the response variable, as shown in

Table 4 Analysis of variance for the screening design

Factors and interactions	DoF	Depth			Volume			Specific wear rate			CoF		
		SS	F	p-Value	SS	F	p-Value	SS	F	p-Value	SS	F	p-Value
A:S	1	184.005	173.42	0.0000	0.116	1183.00	0.0000	96840.3	1242.87	0.0000	0.1430	188.58	0.0000
B:L	1	4420.99	4166.59	0.0000	0.706	7155.90	0.0000	120.333	1.54	0.2603	0.0252	33.24	0.0012
AB	1	178.872	168.58	0.0000	0.022	222.95	0.0000	5633.33	72.30	0.0001	0.0010	1.33	0.2927
Blocks	2	4.22112	1.99	0.2174	0.000	3.32	0.1068	821.16	5.27	0.0477	0.0007	0.47	0.6448
Total error	6	6.36635	0.0005925	467.50	0.0003
Total (corr.)	11	4794.46	0.846732	103883.0	0.0007
R ²	99.86	99.93	99.55	97.39	...
Standard error	1.0300	0.0099	8.8270	0.0275	...
MAE	0.6201	0.0053	5.5555	0.0156	...
Durbin-Watson	2.6472	2.7643	1.3818	2.1472	...
			(P = 0.7219)			(P = 0.7867)			(P = 0.0669)			(P = 0.4053)	

SS, Sum of squares. DoF degrees of freedom. MAE. Mean absolute error

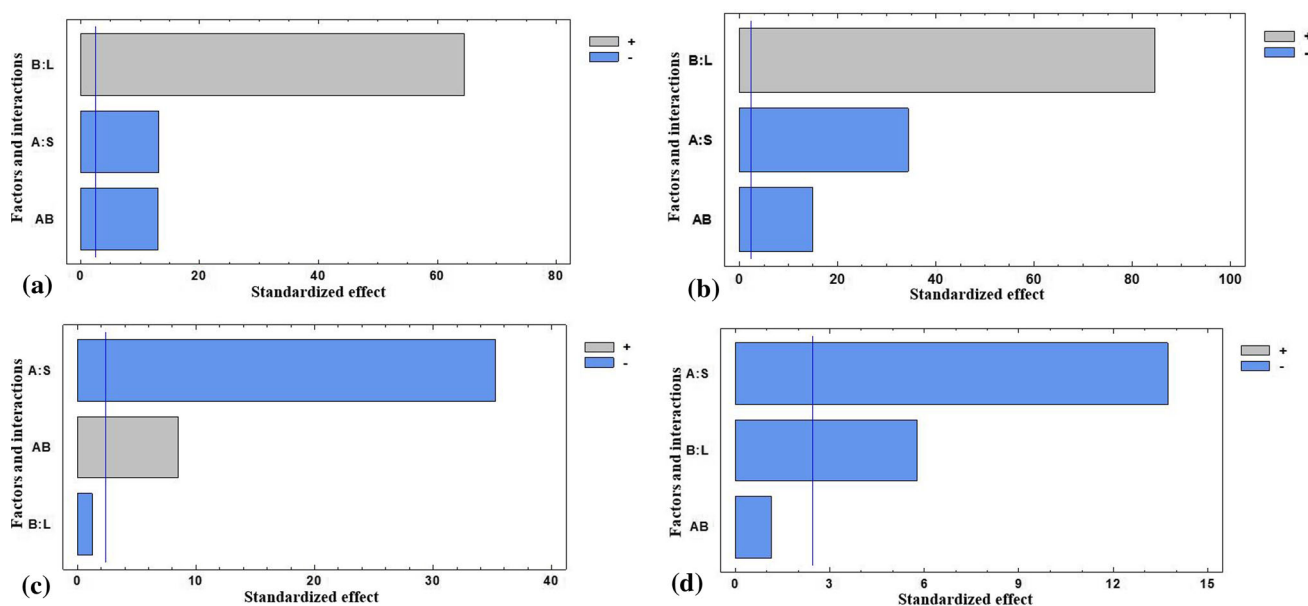


Fig. 4 Pareto plots for cribbed analysis (a) depth, (b) Volume, (c) Specific wear rate, and (d) CoF

Fig. 4(c), this indicates that the correlation coefficient R^2 is low for the statistical model due to the linearity of the experimental results (Ref 20). Figure 4(d) shows that CoF is negatively affected by speed (A:S), as is load (B:L) but to a lesser extent than speed. It is also established that the second-order interaction of the factors (AB) does not influence the behavior of the CoF. Regression models can predict response variables with 95% confidence, as shown in Table 5.

3.1.2 Analysis of Variance for the Response Variables. Table 6 shows the ANOVA results in order to evaluate the statistical significance of the response variables; note that $p \leq 0.05$ expose a high significance of the variables with a compliance level of 95%. It's evident that the factors are highly significant for the response variable CoF and volume. On the other hand, for the depth and specific wear rate variables, there is only the influence of the load factor (B:L). The response variables studied present a correlation coefficient greater than 99% except for the variables CoF and specific wear rate with 97

and 56%, respectively; likewise, the values of the standard error and absolute mean error are observed. The Durbin-Watson (DW) statistic for the response variables studied shows a $p \geq 5\%$, so there is no serial autocorrelation in the residuals.

Figure 5 shows the screening analysis for the design factors where the statistical significance of the factors in the test was determined. Figure 5(a) and (b) shows that the applied load (B:L) is the factor that most positively influences the depth and volume of material removal; likewise, the speed (A:S) has a negative influence, and their interactions have little influence. On the other hand, for the specific wear rate response variable (Fig. 5c), there is a negative influence of the load factor and little influence on the interaction between the factors. Otherwise, it occurs with Fig. 5(d), where the response variable CoF exhibits a negative influence of the load and speed factors, but the interaction between the factors has a positive influence on the values.

Table 5 Comparison between experimental values by block and calculated values

Block	Factors		Experimental values				Calculated values*			
	Speed, mm/s	Load, N	Depth, μm	Volume, $\text{mm}^3 \times 10^{-3}$	Specific wear rate, $\text{mm}^3/\text{Nm} \times 10^{-6}$	CoF	Depth*, μm	Volume*, $\text{mm}^3 \times 10^{-3}$	Specific wear rate*, $\text{mm}^3/\text{Nm} \times 10^{-6}$	CoF*
1	20	5	27.33	126	253	0.62	28.24	127.9	256.76	0.65
	10	10	39.67	309	309	0.65	38.82	320.2	641.02	0.65
	20	20	58.00	483	424	0.51	59.54	517.7	1036.5	0.51
	20	10	38.33	259	259	0.58	38.67	257.9	516.69	0.56
	30	20	57.67	494	247	0.51	57.95	504.0	1009.2	0.52
	10	20	61.67	556	278	0.57	61.13	580.0	1160.8	0.58
	10	5	27.33	192	385	0.74	27.67	190.3	381.10	0.74
	30	10	39.00	246	246	0.55	38.52	244.2	489.36	0.56
	30	5	28.67	104	208	0.65	28.81	114.3	229.43	0.63
2	20	5	30.00	128	257	0.65	28.24	127.9	256.76	0.65
	10	10	39.33	322	323	0.65	38.82	320.2	641.02	0.65
	20	20	59.33	522	261	0.51	59.54	517.7	1036.5	0.51
	20	10	39.00	289	290	0.56	38.67	257.9	516.69	0.56
	30	20	59.00	536	268	0.53	57.95	504.0	1009.2	0.52
	10	20	61.00	611	306	0.58	61.13	580.0	1160.8	0.58
	10	5	26.67	191	383	0.74	27.67	190.3	381.10	0.74
	30	10	38.33	224	225	0.54	38.52	244.2	489.36	0.56
	30	5	28.33	121	244	0.64	28.81	114.3	229.43	0.63

*, are the calculated/predicted values

Table 6 Experimental factors

Factors interactions	and DoF	Depth				Volume			Specific wear rate				CoF	
		SS	F	p-Value	SS	F	p-Value	SS	F	p-Value	SS	F	p-Value	
A:S	1	3.05	3.68	0.0816	0.016	48.78	0.0000	243.00	0.11	0.7517	0.020	113.16	0.0000	
B:L	1	2956.00	3554.10	0.0000	0.450	1329.88	0.0000	21080.50	9.13	0.0116	0.057	323.84	0.0000	
AA	1	0.20	0.24	0.6327	0.003	6.90	0.0235	987.42	0.43	0.5265	0.006	37.62	0.0001	
AB	1	9.68	11.64	0.0058	0.000	0.20	0.6616	6942.86	3.01	0.1107	0.001	5.92	0.0332	
BB	1	0.69	0.84	0.3797	0.000	0.02	0.9038	121.00	0.05	0.8231	0.005	32.91	0.0001	
Blocks	1	0.61	0.74	0.4092	0.001	4.96	0.0478	150.22	0.07	0.8033	0.000	0.13	0.7300	
Total error	11	9.15	0.003	25386.9	0.002	
Total (corr.)	17	3069.87	0.4978	58912.0	0.089	
R ²	99.70	99.24	...	56.90	97.82	...	
Standard error	0.9119	0.0185	...	48.0406	0.0133	...	
MAE	0.5242	0.0118	...	27.3915	0.0074	...	
Durbin-Watson	1.7859	1.5742	...	2.0981	1.9522	...	
			(P=0.2955)			(P=0.1621)		(P=0.5446)				(P=0.4243)		

SS, Sum of squares. DoF degrees of freedom. MAE. Mean absolute error

3.1.3 Regression Model and the Response Surfaces of the Statistical Model. Table 7 shows the regression model for the response variables. Factors and significant interactions were taken into account. The statistical model used is adjusted to the response variables depth, volume, and CoF with a confidence level greater than 97%. It is evident that the response variable specific wear rate does not have a high significance of the results and does not fit the statistical model (42.17%). Thus, the most significant factor is speed. Note that the greatest effect between factors and interactions is the CoF variable.

For the other variables, there is a greater effect of the load except for the specific wear rate and a greater effect of the speed

for volume and specific wear rate except for depth thus, $p \leq 0.05$ with a 95% reliability in the results. The Durbin-Watson (DW) statistic for the response variables studied shows a $p \geq 5\%$, so there is no consecutive autocorrelation in the residuals. Finally, the values of the standard error and absolute mean error are observed. Besides, the DoF values varied due to the statistical behavior of the factors, their interactions, and the statistical significance in the response variable (Ref 27).

Figure 6 shows the behavior of the response variables subjected to the statistical model on response surfaces. These response surfaces show a colored bar that indicates high (Red), medium (green), and low (blue) values for each of the response variables studied. The behavior of the response variables under

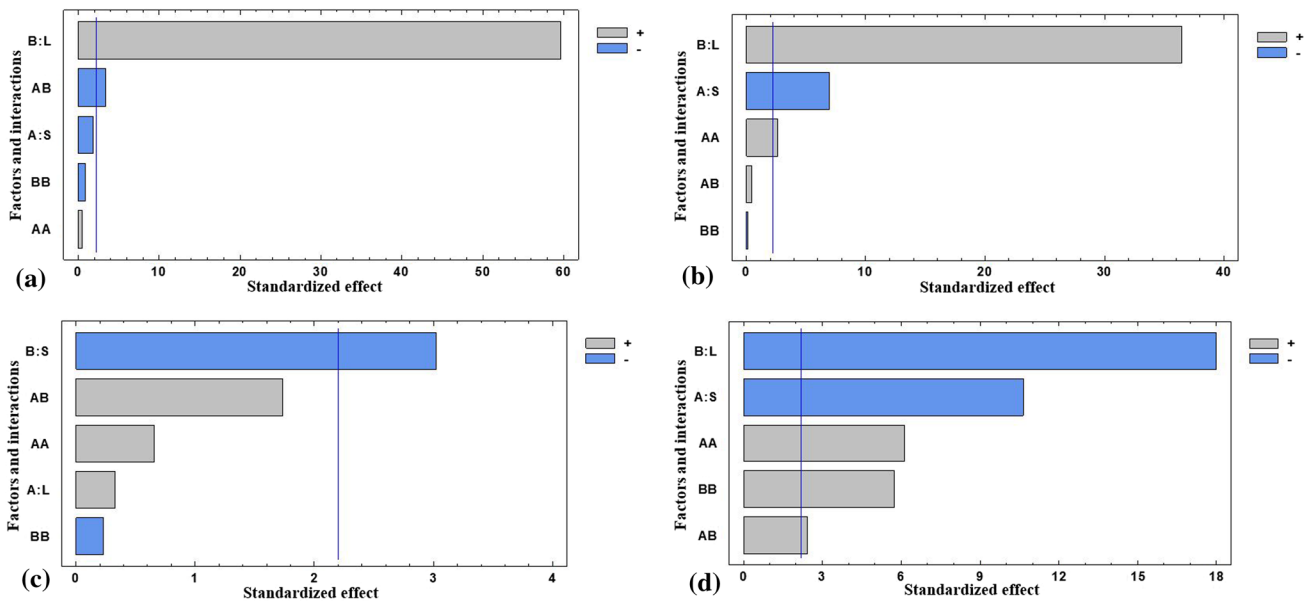


Fig. 5 Pareto plots for (a) depth, (b) Volume, (c) Specific wear rate, and (d) CoF

the test factors is governed by Eq 2, 3, 4 and 5 and plotted in Fig. 6. Note that it results from the regression model for the response variables.

$$\text{Depth} = 15.2217 + (2.37467 \times L) + (0.129125 \times S) - (0.0144036 \times L \times S) \quad (\text{Eq } 2)$$

$$\text{Volume} = 0.171361 + (0.0259833 \times L) - (0.0135333 \times S) + (0.000243333 \times S^2) \quad (\text{Eq } 3)$$

$$\text{Specific wear rate} = 378.0 - (4.55 \times S) \quad (\text{Eq } 4)$$

$$\text{CoF} = 1.05333 - (0.0316667 \times L) - (0.0223333 \times S) + (0.000777778 \times L^2) + (0.00015 \times L \times S) + (0.000408333 \times S^2) \quad (\text{Eq } 5)$$

4. Discussions

4.1 Statistical Results

The correlation of the measured variables and the calculated values by the equations developed by the statistical model were plotted in Fig. 7. Note that correlation coefficient is greater than 97% except for the specific wear rate variable ($R^2=42.17\%$). This low R^2 value might be because the levels of the factors (load and sliding speed) are too narrow, so the effect on the response variable (specific wear rate) when changing from one level to another is too small. Likewise, the tendency of these statistical response surfaces is in agreement with the RSM plots obtained for the experimental values.

In order to evaluate the experimental values versus calculated values, Table 8 was constructed using Eq 2, 3, 4 and 5. Also, an experimental condition of 5 mm/s out of the analysis

was used to corroborate the statistical model. Notice that the error percentage it is less than 20% in some cases, influenced by the load and the experimental conditions, which can be influenced by the behavior of the variable responses; also, with the standard deviation, this percentage decreases. Likewise, the tendency of the response surfaces obtained by statistical analysis agrees with the RSM plots obtained for the experimental values (Ref 10). The response variables behavior is mainly influenced by the failure modes and mechanisms that appear during sliding contact, as to the contribution of the experimental factors involved in the sliding motion. The contribution of the wear failure modes and mechanisms is described in detail in the following section of experimental results for each experimental response variable.

4.2 Experimental Results and 2D Maps

4.2.1 Friction Coefficient. In Fig. 8, the CoF behavior against the relative wear distance for the AISI 316L stainless steel is shown for different sliding speeds and load levels. Common features are observed: there is a short running-in period at the initial stage of the tests (0-10 m) in which the tribological pairs are coupled. At this stage, surfaces may mate better, asperities may be knocked off, or initial films may be worn. This results in the CoF either increasing or decreasing from an initial value. After this stage, the CoF stabilizes into what is called steady-state sliding. For most of the graphs, CoF increases with the relative wear distance, almost converging to a constant value. The fluctuations can be attributed to wear mechanisms and to the appearance of the stick-slip phenomenon, which generates entrapment and expulsion of wear particles (3-body mechanism).

CoF experimental values are summarized in Table 3 and were used to obtain the 2D response surfaces of the CoF in terms of sliding speed and load for the AISI 316L steel samples (Fig. 9). Experimental values are shown as dots in the maps and maximum and minimum values of CoF are indicated. As observed, the critical region in terms of higher values of CoF was found at low load levels and low sliding speeds, which

Table 7 Regression model for the response variables

Factor and interactions	Depth			Volume			Specific wear rate			CoF		
	SS	DoF	F	p-Value	SS	DoF	F	p-Value	SS	DoF	F	p-Value
A:L	3047.72	1	3943.67	0.0000	0.4725	1	1596.22	0.0000
B:S	3.0567	1	3.96	0.0682	0.0173	1	58.53	0.0000	24843.00	1	10.99	0.0047
AA
AB	9.6816	1	12.53	0.0036
BB	0.0023	1	8.00	0.0142
Blocks	0.6123	1	0.79	0.3896	0.0017	1	5.75	0.0323	150.22	1	0.07	0.8001
Total error	10.04	13	0.0038	13	33918.80	15
Total (corr.)	3069.87	17	0.4978	17	58912.00	17
R ²			99.67				99.22				42.17	
Standard error			0.8790				0.0172				47.55	
MAE			0.5992				0.0118				31.3333	
Durbin-Watson			2.0738				1.5444				2.61727	
			(P = 0.4836)				(P = 0.0757)				(P = 0.8580)	
												(P = 0.4243)
SS, Sum of squares. DoF, degrees of freedom. MAE, Mean absolute error												

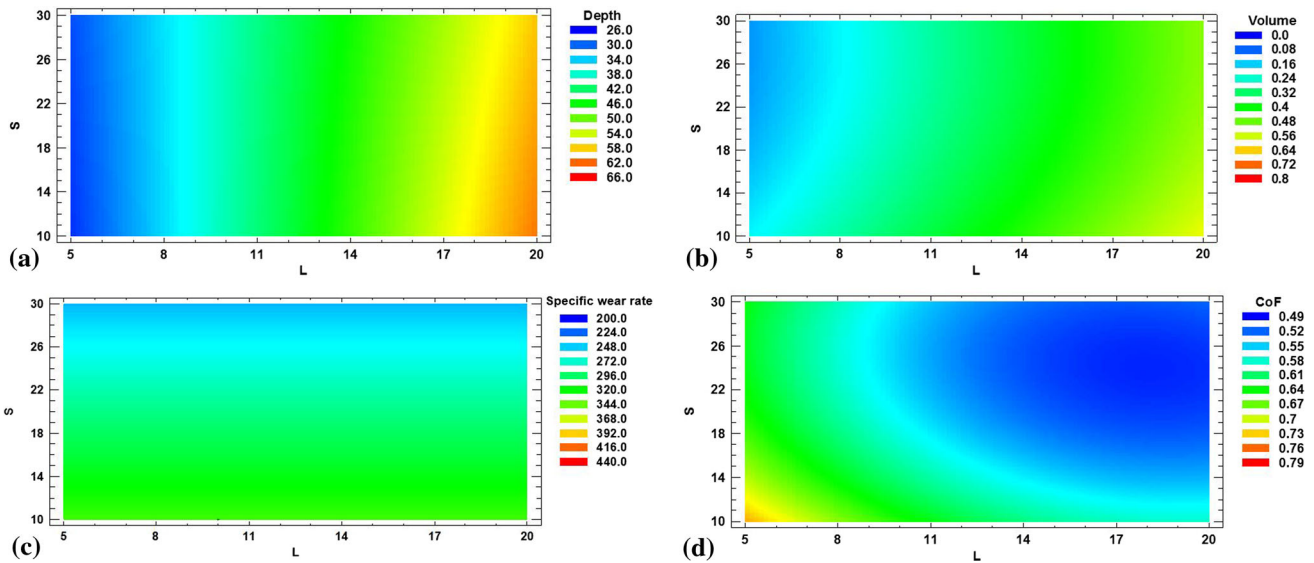


Fig. 6 Response surfaces for (a) depth, (b) Volume, (c) Specific wear rate, and (d) CoF

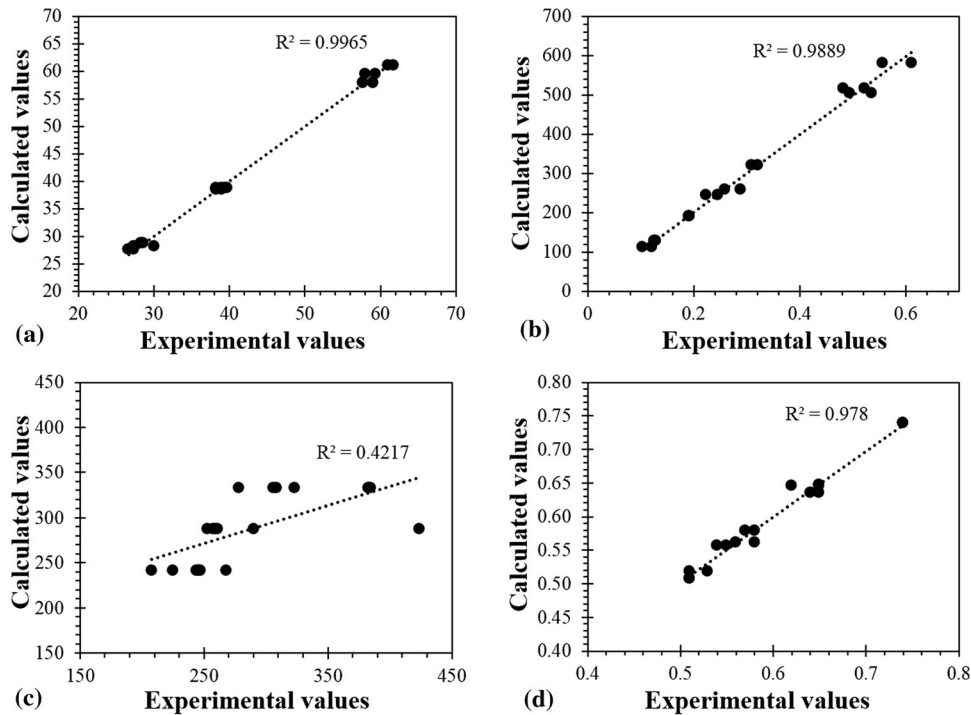


Fig. 7 Estimation of calculated and measured values for (a) Depth, (b) Volume, (c) Specific wear rate, and (d) CoF

might be explained by a change in wear mechanisms (mechanical to chemical) that promotes oxide formation at higher loads and speeds due to elevated temperatures and thus preventing metal-to-metal contact. These results are similar to those reported by (Ref 30,31).

4.2.2 Wear Tracks. Figure 10 shows the cross-sectional views (wear depth and width measurements) of the wear tracks developed under different dry sliding wear conditions at a relative wear distance of 100 m on AISI 316L steel. As observed, the depth and width of the wear tracks had a greater magnitude, indicating a higher material loss. Material removal from a surface via plastic deformation (as expected due to its

low H^3/E^2 ratio equal to 0.001 ± 0.0001) can occur due to deformation failure mechanisms, which include plowing, cutting, and little wedge formation (Ref 5,32). Plowing results in a series of parallel lines as a result of the plastic flow of the softer material. During this process, the material is displaced to the sides, forming ridges as is evident in the edges of the wear track.

Plastic deformation can also be explained by the contact shear stresses generated during the wear tests. According to Tables 3 and 6, the depth of its maximum shear stresses was between ~ 20 to $32 \mu\text{m}$. Also, from Fig. 10, the tracks are more in-depth than this (~ 27 - $74 \mu\text{m}$). Because the maximum shear

Table 8 Error percentage of the experimental versus calculated values

Speed mm/s	Load N	Depth μm	Volume $\text{mm}^3 \times 10^{-3}$	Specific wear rate $\text{mm}^3/\text{Nm} \times 10^{-6}$	CoF ...
5	Experimental values				
	5	27.78 ± 1.77	223.7 ± 6.15	447.4 ± 10.00	0.84 ± 0.021
	10	49.00 ± 1.00	369.7 ± 16.7	369.7 ± 27.20	0.70 ± 0.018
	20	73.89 ± 1.68	794.6 ± 58.3	397.3 ± 9.520	0.76 ± 0.034
	Calculated values				
	5	27.38	239.1	355.25	0.82
	10	38.89	369.6	355.25	0.72
	20	61.92	629.4	355.25	0.64
	Error percentage with the models, %				
	5	1.43	7.06	20.53	1.20
	10	20.63	0.16	3.99	3.85
	20	16.20	20.76	10.59	15.42

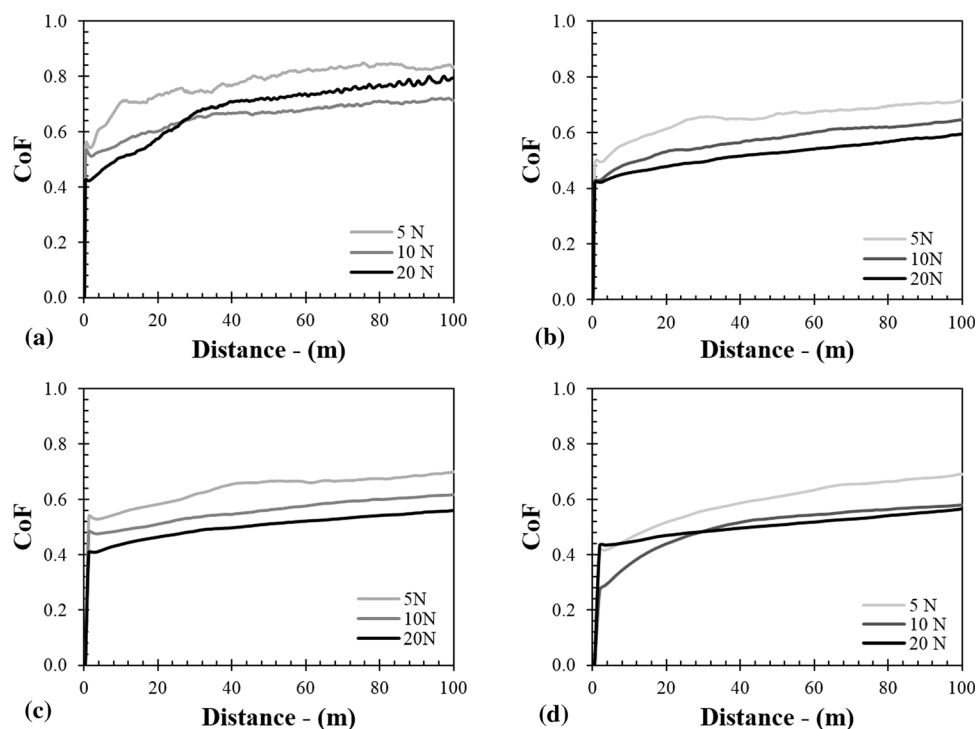


Fig. 8 CoF behavior against relative wear distance AISI 316L steel. (a) 5 mm/s, (b) 10 mm/s, (c) 20 mm/s, and (d) 30 mm/s

stresses (425-674 MPa) exceed the AISI 316L shear stress ($H/6$), localized plastic deformation takes place.

2D maps were obtained with the depth and volume values points shown in Fig. 11 from the experimental values summarized in Table 3. The lower the load, the smaller the wear track (Ref 33). In this way, Fig. 11(b) represents the behavior of the volume material removal obtaining via profilometry. Because the volume increases linearly with the load, it is considered type I according to Straffelini (Ref 29), with a totally adhesive wear mode. However, volume material removal decreases with an increase in the sliding speed, note that a correlation exists between applied load, sliding speed,

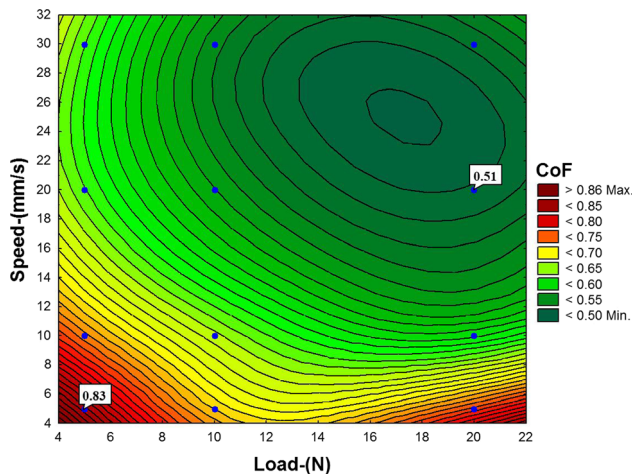


Fig. 9 CoF 2D map for AISI 316L steel under dry sliding wear tests

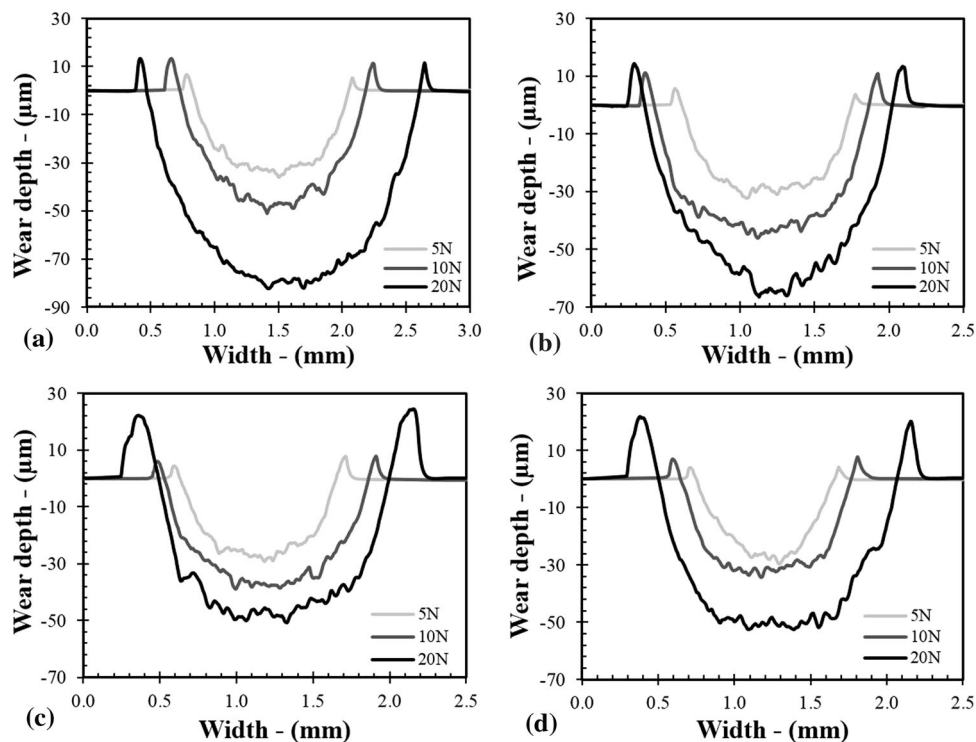


Fig. 10 Cross-sectional views of the wear tracks developed for the AISI 316L steel. (a) 5 mm/s, (b) 10 mm/s, (c) 20 mm/s, and (d) 30 mm/s

and total sliding distance, as has been reported by (Ref 11,20) for the dry sliding wear on the stainless steels.

As defined by Eq 1, the specific wear rate is proportional to the volume of removed material and inversely proportional to the load and total relative distance, which is constant in this case (100 m). Simultaneously, the higher the load, the greater the wear track, and thus, the volume of material removed for the AISI 316L steel (Fig. 11). There are two opposing effects of the load on the specific wear rate, and depending on which failure mechanism prevails, the specific wear rate will increase or decrease with the load. For example, from Fig. 12, in which the 2D map of specific wear rate obtained from experimental values summarized in Table 3, a decrease in specific wear rate for increasing loads at high speeds is observed. Although high loads will imply high volumes of removed material, they can also promote the formation of oxide layers due to higher frictional heating (Ref 33, 34), thus reducing wear. Note that at a certain point, high loads can break the oxide layers and change the wear mechanism.

In conclusion, when metallic materials slide in an oxygen-rich environment, and an increase in the sliding speed often corresponds to a significant decrease in the rate of wear (Ref 33). The maximum specific wear rate was about $\sim 447 \times 10^{-6} \text{ mm}^3/\text{Nm}$, corresponding to the lowest test conditions (S5/L5). In comparison, a minimum value of $\sim 224 \times 10^{-6} \text{ mm}^3/\text{Nm}$ was obtained for the condition (S30/L5). The results are agreed with the ones obtained by Peruzzo et al. (Ref 16), who estimated similar values of wear loss rate, around $70 \times 10^{-6} \text{ mm}^3/\text{Nm}$ at similar experimental conditions.

On the other hand, the decrease in the specific wear rate with sliding speed might be explained by surface strain hardening due to the high plastic deformation generated by the high sliding speeds (similar situation for higher loads). This was previously reported by Lim (Ref 35) for an ultra-mild-wear

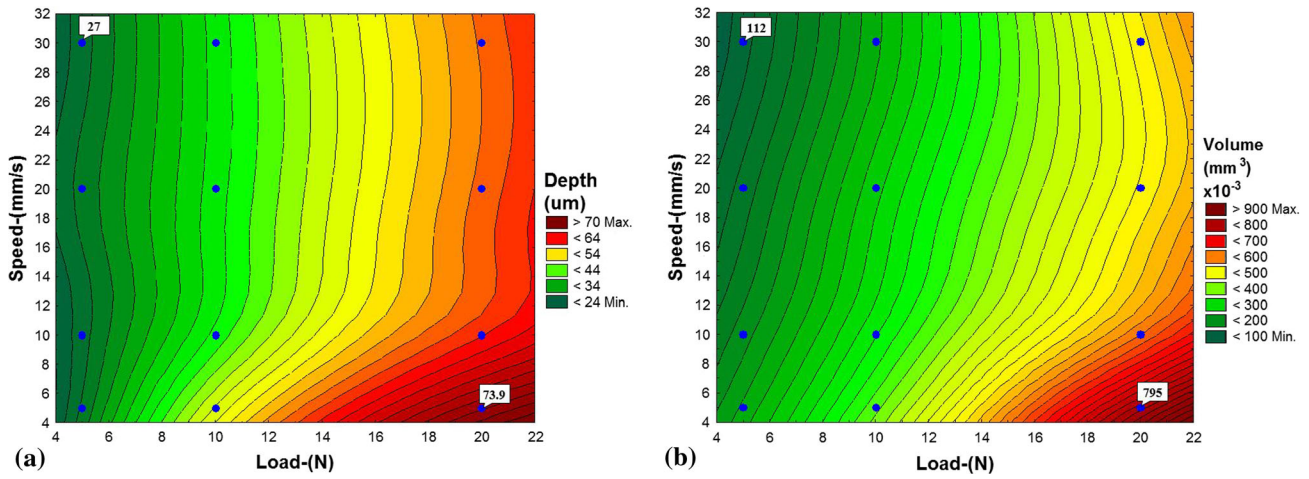


Fig. 11 2D maps for AISI 316L steel under different dry sliding wear conditions. (a) depth, and (b) volume

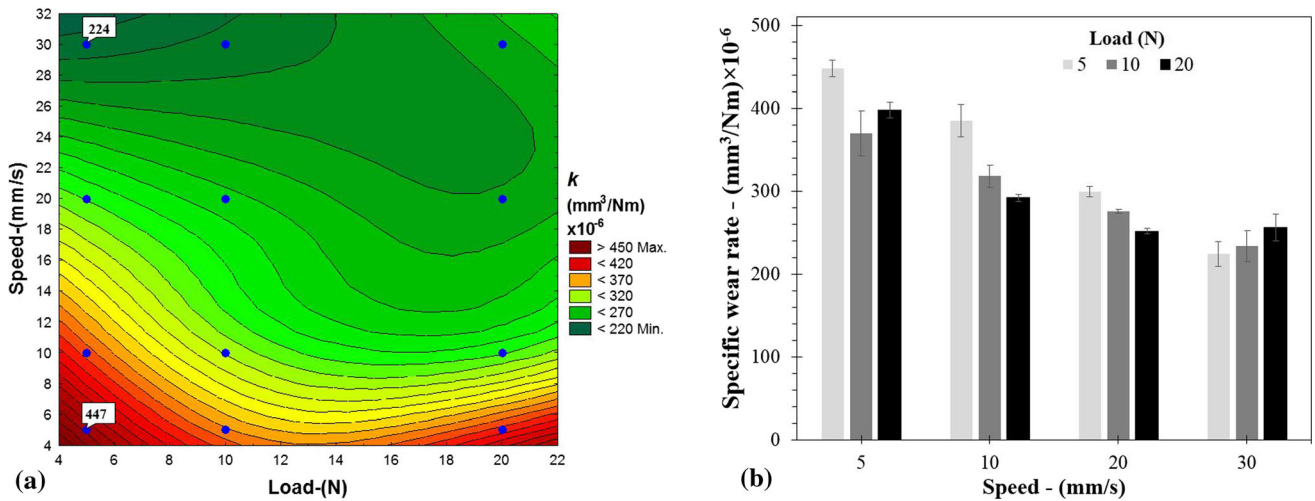


Fig. 12 Specific wear rate for the AISI 316L steel under different dry sliding wear conditions (a) 2D map and (b) behavior in the barplot

regimen. O'Donnell et al. (Ref 17) and Atar (Ref 33) reported an ultra-mild-wear phenomenon for AISI 316L samples under similar conditions, showing a similar behavior of the specific wear rate with the one reported in this work. Also, Thapliyal and Dwivedi (Ref 36) reported that for a ductile alloy with hardness values of 344HV, the highest material wear was obtained at low sliding speeds in a pin-on-disk configuration. For the case of ceramic layers, plastic deformation is limited, there is no surface hardening effect, and thus, their specific wear rate is basically dependent on the volume of material removed: the higher the load and sliding speed, the higher specific wear rate (Ref 19).

4.3 Wear Maps and Failure Mechanisms

Figure 13 shows the SEM micrographs of the worn tracks in which wear mechanisms are indicated using a color code for the severity of the damage: low (green), medium (yellow), and high (red). Maps can be divided into two wear regions: mild and severe with a transition zone. These modes were defined based on the predominant failure mechanisms identified by SEM and

considering the specific wear rate level. From a preliminary analysis, high wear and severe low damage are localized at low sliding speeds and all load levels, while the fewer values of wear are reduced due to strain hardening in sliding speeds higher than 10 mm/s.

During wear tests wear particles (debris) are generated. If the wear particle (debris) is hard, it will damage the softer surface and form a deeper plowing. Otherwise, if the debris has a similar hardness to the surface (Ref 14,37), some of these particles act as 3-body abrasives that wear down the material and formed plowing, which are identified as parallel stripes in the sliding direction, as reported by Peruzzo et al. (Ref 38). The severity of damage generated by the plowing was defined, taking into account the depth, continuity, and parallelism along the sliding direction through qualitative visual analysis of the micrographs. In ceramics, the main wear mechanism is plowing, as reported by Gahr (Ref 39). When the plowing along the sliding direction is not continuous, very smooth, inconspicuous, shallow, and the mechanisms cannot be clearly identified, the polishing failure mechanism appears in some micrographs (Fig. 14); this polishing is observed as a flattening

of the surface, due to the influence of low loads and low speeds. Polished surfaces are generally smooth or shiny, which implies low levels of material removal without plowing, cracks, or visible plastic deformation on the surface (Ref 40).

Material agglomeration occurs when the debris has been reduced to a sufficiently small size, which adheres and clump together due to mechanical contacts on the surface, mainly influenced by the experimental conditions of load and speed.

These agglomerations can evolve and form oxidized compact layers (tribo-film) that provide protection against wear damage. The darker areas of the tribo-film were identified as smearing due to interaction with oxygen from the environment (Ref 41). This tribo-film generates a decrease in the CoF, the volume of removal, and the specific rate of wear (Ref 42).

The surfaces show that plowing and material agglomeration predominate as failure mechanisms during mild wear. Plowing

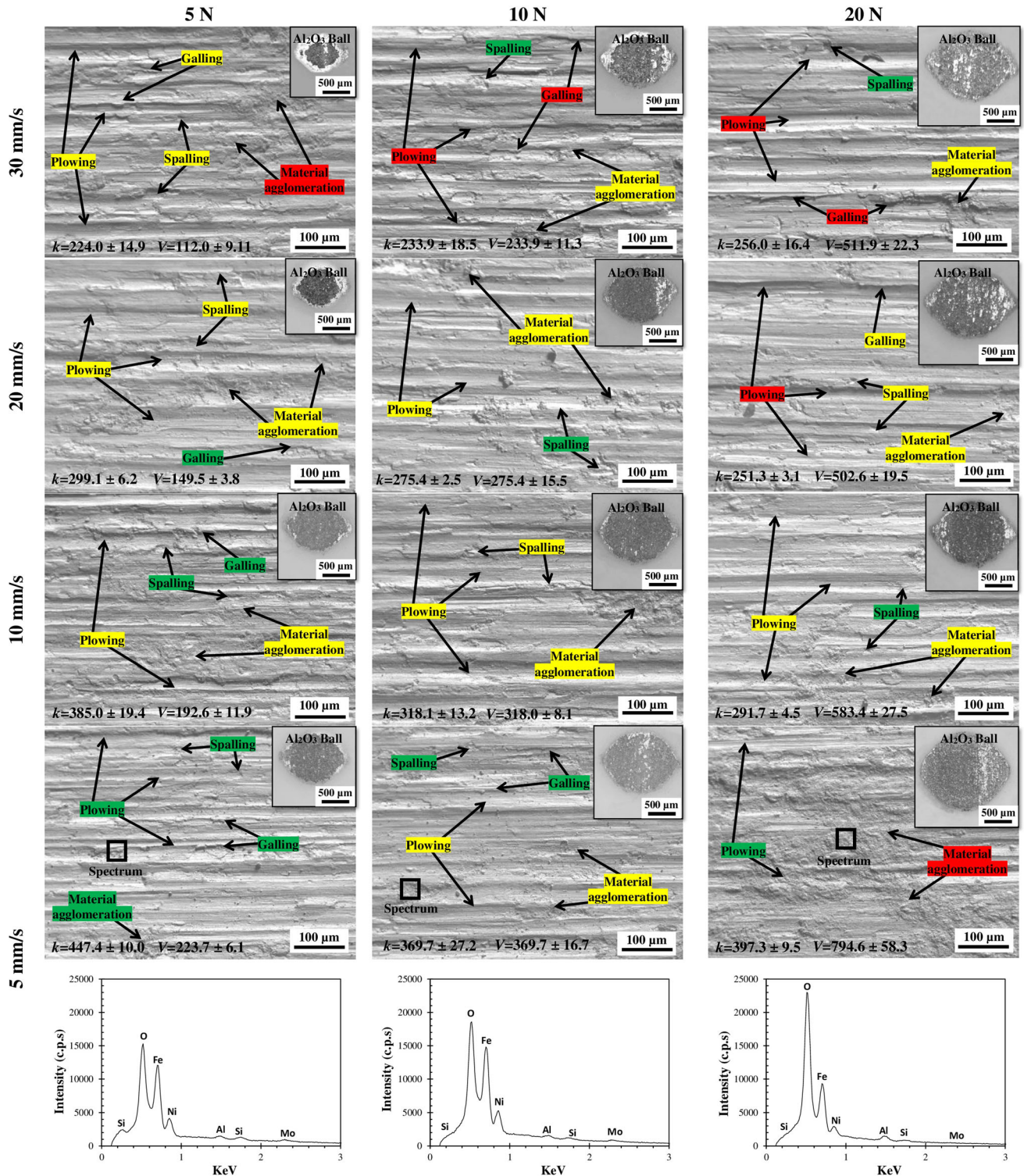


Fig. 13 SEM micrographs of different wear failure mechanisms for all experimental dry sliding wear conditions

is generated by hard particles or debris, which produce the plow on the wear tracks. Note, however, that the depth or severity of the plowing is greater. As the wear regimes change to severe (in the transition zone), the extent of smearing and material agglomeration increases. For severe wear, on the other hand, differences are more evident, with smearing being predominant with plowing and spalling. Also, it shows the spectrum over a specific region of material agglomeration taken from the severe wear regions (region indicated by a rectangle); in the spectra, the presence of iron and nickel oxides generated by the tribochemical effects is identified.

On the other hand, the specific wear rate decreases linearly with increasing hardness, regardless of the production process and the type of material, according to Straffelini (Ref 29). Archard establishes two principles about the specific wear rate: (1) it is independent of the apparent area and is directly proportional to the applied load, and (2) it is constant with the sliding distance (or time) and independent of the speed (Ref 43), and there is a significant influence of sliding speed on worn surface failure mechanisms (Ref 44). There are two opposite effects of load on the specific wear rate, and depending on the dominant failure mechanism, the specific wear rate will increase or decrease depending on the load applied during sliding. Wear mechanisms identified through SEM micrographs (Fig. 13) are summarized in Fig. 14.

According to Fig. 14, the mild wear regions are in:

5 N loads for the entire set of speeds characterized by plowing and some material agglomeration. The volume is low in this region, and the CoF decreases (from 0.83 to 0.63) at high speeds due to strain hardening.

High speeds with loads greater than 10 N under this region the plowing is more pronounced, with some detachment, material agglomeration, and galling due to plastic deformation and strain hardening of the surface, where the lowest CoF value and low values of the specific wear rate are obtained. In this case, the debris is trapped, acting as a 3-body mechanism as reported by (Ref 17) and (Ref 35).

At a certain point, high loads and speeds promote the breakdown of the oxide layer, and the wear mode changes from adhesive to abrasive. The yield stress of the material was considered taking into account the maximum tangential stress theory for ductile materials, which proposes that: $\tau_{Max} \geq (\sigma_y/2)$, using the Tabor relation $\sigma_y = H/3$, with a value of

approximately $(\sigma_y/2) \approx 350$ MPa. In this way, AISI 316L steel presents a relation of $674 \text{ MPa} \geq 350 \text{ MPa}$, concluding that the material failure is by plasticity (Ref 45).

The transition regions to severe wear are found in:

Speeds lower than 10 mm/s for the entire load range it is characterized by mild, less pronounced plowing; with material agglomeration appearing at high loads, providing protection against wear as obtained in the SEM-EDS with the presence of the alloying elements. Notice that high oxygen contents were detected on the worn surfaces, which exposed Fe_2O_3 and Fe_3O_4 phases or FeO-based iron according to (Ref 46), which aid to reduce the specific wear rate (Ref 47).

In this region, the specific wear rate and CoF are high (0.70-0.83); this behavior was previously reported by (Ref 17, 36). According to (Ref 48) at speeds less than 100 mm/s, there is no significant heating of the surface, and wear occurs due to cold mechanisms such as plasticity and tribochemical effects.

In Fig. 15, wear track edges are shown. It is evident the direct contribution of oxidation to the progression of wear (Ref 18, 49). As mentioned previously, oxide islands generated during sliding contact can minimize the mechanical contact between the counterpart and the steel, reducing material transfer to the counter-face. Also, it is observed that the evolution of the plastic deformation on the wear track edge increase when the sliding speed decrease for low loads, but when the load and sliding speed increase, the plastic deformation on the edges increases too, as was identify via optical profilometry (See Fig. 10). From the EDS spectra, the main contribution of oxide and iron and alloying elements during sliding wear is evident.

5. Conclusions

The main conclusions about the wear maps and statistical approach of AISI 316L alloy under dry sliding conditions obtained in the previous study are reported as follows:

- The statistical analysis showed that the load influences the depth, volume, and CoF response variables in a positive way with more than 97% of confidence; while the specific wear rate response variable is mainly affected by the sliding speed with more than 42% of confidence.
- It was possible to obtain statistical equations to predict and approach the behavior of the response variables taking into account the factors and levels; this approach is susceptible to the standard deviation that occurs due to the effects of the environment and performance of the failure mechanism during dry sliding wear tests.
- 2D wear maps on AISI 316L steel were obtained to elucidate the role of dry sliding parameters on specific wear rate and wear regimes during reciprocating wear tests. The maximum specific wear rate was $\sim 450 \times 10^{-6} \text{ mm}^3/\text{Nm}$, corresponding to the lowest test conditions: 4 N and 4 mm/s, whereas a minimum value of $\sim 220 \times 10^{-6} \text{ mm}^3/\text{Nm}$ was obtained for the condition of 12 N and 32 mm/s. A decrease in specific wear rate for increasing loads at high speeds is observed in the AISI 316L steel, which is explained by the oxide formation that could minimize the contact between the counterpart and the steel, thus reducing wear.
- SEM-EDS analysis confirmed the influence of the sliding speed on the failure mechanism and the specific wear rate.

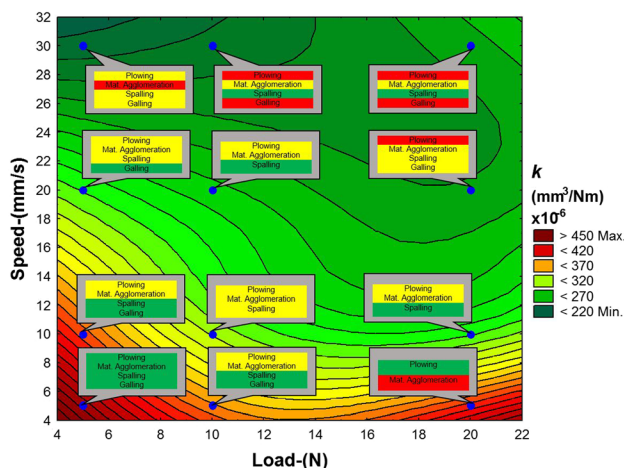


Fig. 14 2D wear map indicating wear regimes for AISI 316L steel under different dry sliding wear conditions

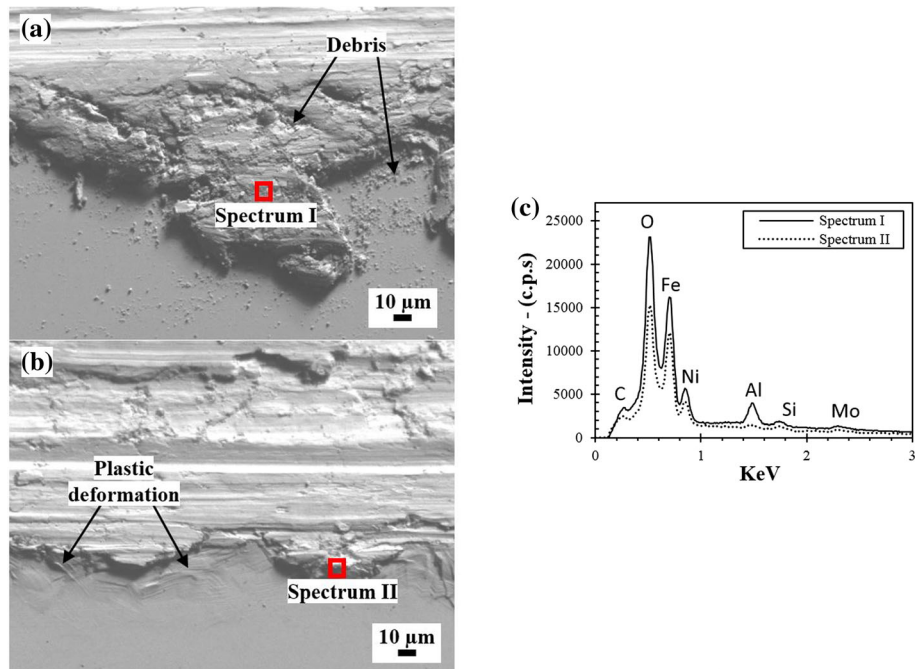


Fig. 15 Wear track edge for the AISI 316L steel for (a) S5/L5 condition, (b) S20/L5 condition, and (c) EDS spectra

Therefore, the decrease in specific wear rate with sliding velocity in the AISI 316L steel might be explained by surface hardening due to the high plastic deformation generated by the high sliding speeds. On the worn track, plowing and material agglomeration predominates as failure mechanisms during mild wear. For the mild and transition regions, failure modes are similar to those reported in some references. For severe wear, on the other hand, differences are more evident, with smearing being predominant.

- Higher specific wear rates for the AISI 316L steel are also promoted by its higher values of CoF, which is explained by its lower hardness that allows a deeper penetration of the counterpart, and by its higher levels of plastic deformation (lower H^3/E^2 ratio), both of which promotes a better coupling between counterpart and surface, and thus generating higher values of CoF.

Acknowledgments

This work was supported by the research grant 2021111 of the Instituto Politécnico Nacional of México. R.A. García-León thanks Dr. Hugo Martínez (Centro de Nanociencias y Nanotecnologías del IPN) for his support on the SEM-EDS analysis.

Author contribution

R.A. García-León, Investigation, Methodology, Formal Analysis, Original Draft, Writing-Review & Editing. J. Martínez-Trinidad, Methodology, Project Administration, Supervision, Formal Analysis, Funding Acquisition. A. Guevara-Morales, Conceptualization, Methodology, Formal Analysis, Supervision, Writing-

Review. I. Campos-Silva, Methodology, Supervision, other contributions. U. Figueroa-López, Methodology, Supervision, other contributions.

Conflict of interest

The authors declared that they have no conflicts of interest to this work.

References

1. R.K. Gupta, and N. Birbilis, The Influence Of Nanocrystalline Structure and Processing Route on Corrosion of Stainless Steel: A Review, *Corros. Sci.*, 2015, **92**, p 1–15. <https://doi.org/10.1016/j.corsc.2014.11.041>
2. A.M. Kumar, and N. Rajendran, Influence of Zirconia Nanoparticles on the Surface and Electrochemical Behaviour of Polypyrrole Nanocomposite Coated 316L SS in Simulated Body Fluid, *Surf. Coat. Technol.*, 2012, **213**, p 155–166. <https://doi.org/10.1016/j.surfcoat.2012.10.039>
3. M.A. Hussein, A.S. Mohammed, N. Al-aqeeli, and S. Arabia, Wear Characteristics of Metallic Biomaterials: A Review, *Mater. (Basel)*, 2015, **8**(1), p 2749–2768. <https://doi.org/10.3390/ma8052749>
4. I. Hutchings, and P. Shipway, *Sliding Wear*, 2nd ed. Elsevier Ltd., Amsterdam, 2017
5. B. Bhushan, *Principles and Applications of Tribology*, Tribology, Wiley, Estados Unidos, 1999
6. K. Sadiq, M.M. Stack, and R.A. Black, Wear Mapping of CoCrMo Alloy in Simulated Bio-tribocorrosion Conditions of a Hip Prosthesis Bearing in Calf Serum Solution, *Mater. Sci. Eng.*, 2015, **49**, p 452–462. <https://doi.org/10.1016/j.msec.2015.01.004>
7. B. Bhushan, *Modern Tribology Handbook*, Vol One CRC Press, USA, 2001
8. G. Rasool, and M.M. Stack, Wear Maps for TiC Composite Based Coatings Deposited on 303 Stainless Steel, *Tribol. Int.*, 2014, **74**, p 93–102. <https://doi.org/10.1016/j.triboint.2014.02.002>
9. M.B. Maros, and A.K. Németh, Wear Maps of HIP Sintered Si3N4/MLG Nanocomposites for Unlike Paired Tribosystems Under Ball-On-

- Disc Dry Sliding Conditions, *J. Eur. Ceram. Soc.*, 2017, **37**(14), p 4357–4369. <https://doi.org/10.1016/j.jeurceramsoc.2017.05.005>
10. M. Davanageri, S. Narendranath, and R. Kadoli, Dry Sliding Wear Behavior of Super Duplex Stainless Steel AISI 2507: A Statistical Approach, *Arch. Foundry Eng.*, 2016, **16**(4), p 47–56. <https://doi.org/10.1515/afe-2016-0082>
 11. S. Basavarajappa, and G. Chandramohan, Dry Sliding Wear Behavior of Metal Matrix Composites: A Statistical Approach, *J. Mater. Eng. Perform.*, 2006, **15**(6), p 656–660. <https://doi.org/10.1361/105994906X150731>
 12. S. Baskaran, and V. Anandkrishnan, Statistical Analysis of Coefficient of Friction During Dry Sliding Wear Behaviour of TiC Reinforced Aluminium Metal Matrix Composites, *Mater. Today Proc.*, 2018, **5**(6), p 14273–14280. <https://doi.org/10.1016/j.matpr.2018.03.009>
 13. B. Saleh et al., Statistical Analysis of Dry Sliding Wear Process Parameters for AZ91 Alloy Processed by RD-ECAP Using Response Surface Methodology, *Met. Mater. Int.*, 2020 <https://doi.org/10.1007/s12540-020-00624-w>
 14. P.L. Menezes, S.P. Ingole, M. Nosonovsky, S.V. Kailas, and M.R. Lovell, *Tribology for Scientists and Engineers*, Springer, New York USA, 2013
 15. J.L. Montes-Seguedo et al., Mapping the Friction Coefficient of AISI 316L on UHMWPE Lubricated with Bovine Serum to Study the Effect of Loading and Entrapment at High Values of Sliding-to-rolling Ratio, *Health Technol. (Berl)*, 2019, **10**, p 385–390. <https://doi.org/10.1007/s12553-019-00355-y>
 16. M. Peruzzo, F.L. Serafini, M.F.C. Ordonez, R.M. Souza and M.C.M. Farias, Reciprocating Sliding Wear of the Sintered 316L Stainless Steel with Boron Additions, *Wear*, 2019, **422–423**, p 108–118
 17. L.J. O'Donnell, G.M. Michal, F. Ernst, H. Kahn, and A.H. Heuer, Wear Maps for Low Temperature Carburised 316L Austenitic Stainless Steel Sliding Against Alumina, *Surf. Eng.*, 2010, **26**(4), p 284–292. <https://doi.org/10.1179/026708410X12550773057901>
 18. M.C.M. Farias, R.M. Souza, A. Sinatora, and D.K. Tanaka, The Influence of Applied Load, Sliding Velocity and Martensitic Transformation on the Unlubricated Sliding Wear of Austenitic Stainless Steels, *Wear*, 2007, **263**(1–6), p 773–781. <https://doi.org/10.1016/j.wear.2006.12.017>
 19. R.A. García-León, J. Martínez-Trinidad, I. Campos-Silva, U. Figueroa-López, and A. Guevara-Morales, Wear Maps of Borided AISI 316L Steel Under Ball-on-Flat Dry Sliding Conditions, *Mater. Lett.*, 2021, **282**, p 128842. <https://doi.org/10.1016/j.matlet.2020.128842>
 20. R.A. García-León et al., Dry Sliding Wear Test on Borided AISI 316L Stainless Steel Under Ball-on-Flat Configuration: A Statistical Analysis, *Tribol. Int.*, 2021, **157**, p 106885. <https://doi.org/10.1016/j.triboint.2021.106885>
 21. R.A. García-León, J. Martínez-Trinidad, I. Campos-Silva, and W. Wong-Angel, Mechanical Characterization of the AISI 316L Alloy Exposed to Boriding Process, *Dyna (Colombia)*, 2020, **87**(213), p 34–41
 22. Acequisa, “Aceros y Equipos S.L. Aleación AISI 316L,” Online, 2018. <http://acequisa.com/spanish/inox/316l.html>
 23. A. Jana et al., Severe Wear Behaviour of Alumina Balls Sliding Against Diamond Ceramic Coatings, *Bull. Mater. Sci.*, 2016, **39**(2), p 573–586. <https://doi.org/10.1007/s12034-016-1166-2>
 24. K. Holmberg, and A. Matthews, *Coatings Tribology: Properties, Mechanisms, Techniques and Applications in Surface Engineering*, Elsevier, United Kingdom, 2009
 25. G.B. Stachowiak, M. Salasi, W.D.A. Rickard, and G.W. Stachowiak, The Effects of Particle Angularity on Low-Stress Three-Body Abrasion-Corrosion of 316L Stainless Steel, *Corros. Sci.*, 2016, **111**, p 690–702. <https://doi.org/10.1016/j.corsci.2016.06.008>
 26. H. Gutiérrez Pulido, and R. De La Vara Salazar, *Análisis y Diseño de Experimentos*, McGraw-Hil, Mexico, 2015
 27. D. Montgomery, and G. Runger, *Applied Statistics and Probability for Engineers*, WILEY, United States of America, 2018
 28. S.A. Selvan, and S. Ramanathan, Dry Sliding Wear Behavior of Hot Extruded ZE41A Magnesium Alloy, *Mater. Sci. Eng. A*, 2010, **527**(7–8), p 1815–1820. <https://doi.org/10.1016/j.msea.2009.11.017>
 29. G. Straffelini, Wear Mechanisms. Friction and Wear, *Springer Tracts Mech. Eng.*, 2015, **11**, p 85–113. https://doi.org/10.1007/978-3-319-05894-8_4
 30. C.D. Resendiz-Calderon, L.I. Farfan-Cabrera, J.E. Oseguera-Peña, I. Cázares-Ramírez, and E.A. Gallardo-Hernandez, Friction and Wear of Metals Under Micro-abrasion, Wet and Dry Sliding Conditions, *J. Mater. Eng. Perform.*, 2020, **29**(9), p 6228–6238. <https://doi.org/10.1007/s11665-020-05102-3>
 31. K. Benarji, Y. Ravi Kumar, A.N. Jinoop, C.P. Paul, and K.S. Bindra, Effect of Heat-Treatment on the Microstructure, Mechanical Properties and Corrosion Behaviour of SS 316 Structures Built by Laser Directed Energy Deposition Based Additive Manufacturing, *Met. Mater. Int.*, 2020 <https://doi.org/10.1007/s12540-020-00838-y>
 32. C. Li, X. Deng, L. Huang, Y. Jia, and Z. Wang, Effect of Temperature on Microstructure, Properties and Sliding Wear Behavior of Low Alloy Wear-Resistant Martensitic Steel, *Wear*, 2019 <https://doi.org/10.1016/j.wear.2019.203125>
 33. E. Atar, Sliding wear performances of 316 L, Ti6Al4V, and CoCrMo alloys, *Kov. Mater.*, 2013, **51**, p 183–188. <https://doi.org/10.4149/km-2013-3.183>
 34. K. Holmberg, and A. Matthews, *Coatings Tribology, Second Edition: Properties, Mechanisms, Techniques and Applications in Surface Engineering*, Elsevier, United Kingdom, 2009
 35. S. C. Lim, “Wear Maps.” In ASM Handbook, Volume 18, Friction, Lubrication, and Wear Technology George E. Totten, editor, vol. 18, 2017, pp. 233–243
 36. S. Thapliyal, and D.K. Dwivedi, Study of the Effect of Friction Stir Processing of the Sliding Wear Behavior of Cast NiAl Bronze: A Statistical Analysis, *Tribol. Int.*, 2016, **97**, p 124–135. <https://doi.org/10.1016/j.triboint.2016.01.008>
 37. D.A. Rigney, M.G.S. Naylor, R. Divakar, and L.K. Ives, Low Energy Dislocation Structures Caused by Sliding and by Particle Impact, *Mater. Sci. Eng.*, 1986, **81**, p 409–425. [https://doi.org/10.1016/0025-5416\(86\)90279-X](https://doi.org/10.1016/0025-5416(86)90279-X)
 38. M. Peruzzo, F.L. Serafini, M.F.C. Ordoñez, R.M. Souza, and M.C.M. Farias, Reciprocating Sliding Wear of the Sintered 316L Stainless Steel with Boron Additions, *Wear*, 2019, **423**, p 108–118. <https://doi.org/10.1016/j.wear.2019.01.027>
 39. K.-H. Z. B. T.-T. S. Gahr, Ed., “Chapter 5. Grooving Wear” In *Microstructure and Wear of Materials*, vol. 10, Elsevier, 1987, pp. 132–350
 40. J.R. Davis, *Surface Engineering for Corrosion and Wear Resistance*, ASM Intern, United States of America, 2001
 41. J. Jiang, F.H. Stott, and M.M. Stack, The Role of Triboparticulates in Dry Sliding Wear, *Tribol. Int.*, 1998, **31**(5), p 245–256
 42. K. Kato, and K. Adachi, Wear of Advanced Ceramics, *Wear*, 2002, **253**, p 1097–1104
 43. B. Bhushan, *Introduction to Tribology*, Second Ed. New York, USA, 2013
 44. K. Adachi, K. Kato, and N. Chen, Wear Map of Ceramics, *Wear*, 1997, **203–204**, p 291–301. [https://doi.org/10.1016/S0043-1648\(96\)07363-2](https://doi.org/10.1016/S0043-1648(96)07363-2)
 45. T.E. Fischer, M.P. Anderson, and S. Jahanmir, Influence of Fracture Toughness on the Wear Resistance of Yttria-Doped Zirconium Oxide, *J. Am. Ceram. Soc.*, 1989, **72**(2), p 252–257. <https://doi.org/10.1111/j.1151-2916.1989.tb06110.x>
 46. H.Y. Lee, Effect of Changing Sliding Speed on Wear Behavior of Mild Carbon Steel, *Met. Mater. Int.*, 2020, **26**(12), p 1749–1756. <https://doi.org/10.1007/s12540-019-00417-w>
 47. K.-H. Gahr, “Chapter 6. Sliding Wear,” in *Microstructure and Wear of Materials*, vol. 10, 1987, pp. 351–495
 48. M.F. Ashby, and S.C. Lim, Wear-Mechanism Maps, *Scr. Metall. Mater.*, 1990, **24**(5), p 805–810. [https://doi.org/10.1016/0956-716X\(90\)90116-X](https://doi.org/10.1016/0956-716X(90)90116-X)
 49. N. Lin et al., A Combined Surface Treatment of Surface Texturing-Double Glow Plasma Surface Titanizing on AISI 316 Stainless Steel to Combat Surface Damage: Comparative Appraisals of Corrosion Resistance and Wear Resistance, *Appl. Surf. Sci.*, 2019, **493**, p 747–765. <https://doi.org/10.1016/j.apsusc.2019.06.028>

Publisher's Note Springer Nature remains neutral with regard to jurisdictional claims in published maps and institutional affiliations.